39th AIAA Fluid Dynamics Conference
22 - 25 June 2009, San Antonio, Texas

AIAA 2009-3568

Study of the Bow Shock Interaction with Laser-Pulse-Heated Air Bubbles

Erich Schülein*
German Aerospace Center DLR, Institute of Aerodynamics and Flow Technology,
37073 Göttingen, Germany

Alexander A. Zheltovodov†, Evgeny A. Pimonov‡, Maxim S. Loginov§
Khristianovich Institute of Theoretical and Applied Mechanics SB RAS
630090 Novosibirsk, Russia

The influence of various parameters characterizing the single- and double-pulse energy deposition (ED) upstream of a blunt body (distance between the deposition point and the body, amount of the energy and time delay between the pulses) on the topology of the supersonic flow at Mach 2 is studied experimentally and numerically. The obtained pressure-time diagram at the upstream stagnation point of the body as well as some significant topological properties of the bow-shock / heated-bubble interaction, like shock deformation and reflection, as well as the evolution of the heated bubble into vortex rings downstream, are analyzed as resulting from the shock-decelerated spherical *light-gas* inhomogeneity. The evolution and topology of the interfering heated bubbles by double-pulse ED show the significance of vorticity generation initiated by blast-waves coming from the neighboring bubbles.

Nomenclature

A	Atwood number
B, C, D	peaks in the time-history of the surface pressure record (Figure 13)
D	diameter of the body
E_{ED}	energy per pulse
L_{ED}	distance between the energy deposition location and the body
M	Mach number
p_1	static pressure upstream of the shock wave
p_2	static pressure behind shock wave
Re	Reynolds number
t	time after the discharge
w	vorticity
Δt_{ED}	time interval between two pulses
ϵ_{ED}	ratio of absorbed energy per laser pulse
ρ_1	density upstream of the shock wave
ρ_b	bubble gas density upstream of the shock wave

*Research Scientist, Department High Speed Configurations, erich.schuelein@dlr.de, Member AIAA
†Senior Scientist, Associate Fellow AIAA
‡Research Scientist
§Research Scientist

I. Introduction

Flow control by energy deposition (ED) is the object of investigations at least since the middle of the last century. Already the earlier experimental investigations[1] show that, similar to the effect of a conventional solid aero-spike, the steady localized flow heating upstream of a supersonic blunt body can dramatically reduce its wave drag. Moreover, the effect of a conventional aero-spike could be additionally increased in these experiments by external hydrogen combustion inside of the spike-induced separation. Today, it is well-known[2−8] that the flow control by ED can be applied in high-speed flows to achieve some positive global aerodynamic effects (drag reduction, lift and moments control), or to minimize some negative flow features, like local peaks in pressure and heating loads. Especially the remote control of flows using microwave or optical discharge (OD) by focusing a laser beam upstream of the body (Figure 1), is recently of highest scientific interest. The important finding here was the numerically predicted[9] and confirmed later in wind-tunnel experiments[10,11] possibility to use the unsteady flow heating by pulsed high-repetitive ED for drag reduction. In the last ten years, the number of annual publications about ED for flow control has climbed suddenly. Surveys of the major experimental and numerical investigations can be found in Refs. 2-8.

The success of the simplified numerical models, mostly based on the Euler equations, in the prediction of the flow topology of the interaction of the heated bubble with a bow shock, demonstrates that the parameters related to real-gas or plasma effects could not be dominant therewith (see, e.g. Refs.12-16). For instance, the transformation of a heated bubble created by OD during the bow-shock interaction upstream of a sphere at $M = 3.45$, accompanied by the appearance of secondary rarefaction and shock waves and observed experimentally,[17] could be predicted in this way numerically in some details.[16] The basic effect seems to be the inhomogeneity of gas-dynamic parameters, induced by the localized flow heating.[12] Due to the temperature increasing some important flow parameters, like Mach number, stagnation pressure and density are clearly decreased, whereas the sonic speed is correspondingly increased inside of the bubble.

The unsteady flow that happens when a traveling shock wave hits a spherical density inhomogeneity in quiescent gaseous environment, e.g. by the passage of a planar shock wave across a He-bubble embedded in air, is known as the classical shock / bubble interaction (SBI). Shock-accelerated inhomogeneous flows and, especially, the SBI are the object of intensive investigations in the last 40-50 years and their topology seems to be well understood. The most recent review of these investigations can be found, e.g., in Ref.18. The SBI flow is characterized by the Atwood number defining as $A = (\rho_b - \rho_1) / (\rho_b + \rho_1)$, where ρ_1 is the ambient gas density and ρ_b is the bubble gas density, both before the interaction. The *light*-bubble case takes place at $A < 0$. This case is referred to also as *slow-fast-slow* case,[19] because at uniform specific heats the sound speed of the ambient gas is lower than that of the bubble gas. The instability of the bubble interface by impulsive acceleration due to shock-wave passage is in general known as Richtmyer-Meshkov (RM) instability.

The most common appearance of the RM-instability occurs when the shock wave passes through the perturbed interface between two gases of different densities (Figure 2).[20] The acceleration of both gases by the shock wave causes the growth of initial periodic perturbations, which begin to increase in amplitude. The mutual penetration of the *light* (1) and *heavy* (2) gases leads to formation of some *spike-like* and *bubble-like* structures. Finally, the vortex sheet rolls up and accumulates into periodic vortex cores in the post-shock flow. The mechanism of this *baroclinic* vorticity generation is based on the misalignment of the existing density gradient across the bubble surface and the shock-induced pressure gradient according to the two-dimensional, compressible vorticity equation,[20]

$$\rho \frac{D}{Dt} \frac{w}{\rho} = \frac{\nabla\rho \times \nabla p}{\rho^2}$$

where w is the vorticity vector directed normal to the plane including the pressure- and density-gradient vectors.

The evolution of the flow topology by the classical interaction of a strong plane shock wave with a light-gas bubble[18,21] is sketched in Figure 3. The shock-bubble interaction is similarly mainly determined by some interconnected processes of shocked acceleration / compression of the light-gas bubble accompanied by the mentioned baroclinic vorticity generation. The vectors of corresponding density and pressure gradients are shown in Figure 3(a) by arrows. The shock wave is refracted during the interaction with the curved surface of the inhomogeneity and becomes convex inside of the bubble (b). The compression of the light-gas bubble behind the transmitted shock wave leads to the formation of secondary rarefaction waves, traveling opposite to the main shock direction. Furthermore, due to the interaction of the transmitted shock wave with the inner surface of the bubble, additional shock waves emerge, which are reflected back afterward the

rarefaction waves (c). The RM-instability of the bubble interface is responsible for the formation of a series of long-living vortex rings in the post-shock flow (d).[21]

Similar details of the formation of the secondary rarefaction and compression waves during the passage of the heated bubble through the bow shock were clearly determined in some earlier numerical investigations, addressed to the unsteady interaction of a spherical-nosed body with a finite temperature inhomogeneity in the oncoming uniform flow (see e.g. Ref. 12). The processes of the heated bubble deformation behind the bow-shock, as well as of the vorticity generation during the interaction, were discussed in this paper in detail. The clear benefit of a simplified consideration of these phenomena in the framework of classical SBI, in comparison to the bow-shock interaction with laser-pulse-heated air bubbles, is the absence of the body in the post-shock flow. By the presence of a body some additional waves, reflecting from its surface, complicate furthermore the flow topology and its causal research.

The normal shock interaction in a channel flow is another case, where the shock-bubble interaction occurs without a body's presence. Figure 4 shows some results[14,15] obtained numerically by means of a perfect-gas Euler-equation model, which demonstrate specific stages of a similar channel flow interaction. The deposited energy level is characterized here by the ϵ_{ED}, defined as the ratio of the absorbed energy per pulse to the free-stream enthalpy in the initial volume of the energy source. The coordinates x and y are normalized by the channel height H. The computed flow-field structure is, for the most part, similar to the one demonstrated in Figure 3. A sole exception, which is relatively insignificant for the interaction at these stages, is the presence of the blast wave (1) caused by the initially explosion of the pulse-heated bubble (2) (Figure 4, a) and reflected later back from the channel walls (6) (Figure 4, e, f). Some additional details of the realized flow-field structure, such as the deformation of the shock front (3) with appearance of triple points and shear-layer surfaces spreading from them, the reflected re-transmitted crossing shock waves (5), the primary (7) and secondary (8) vortex structures downstream, are very similar to that of the classical SBI.

A very interesting additional phenomenon, occurring after the short-pulse OD, is the possibility to generate vorticity in the expanding flow even without interaction with an external shock wave. The experimental and computational study of the flow, induced by the explosion of a pulse-heated bubble,[22] shows that the shape of the energy source plays an important role in the resulting flow topology. The momentum transferred to the heated air at a non-spherical blast wave is anisotropic, resulting in the emergence of a *reversal subsonic jet* flow along the axis of symmetry after the explosion. The second effect, analyzed in the cited paper, is the baroclinic vorticity generation, occurring in the presence of a solid wall, due to interaction of the blast wave, reflected from this surface, with the heated gas during the early stage of the explosion. This effect works contrary to the mentioned anisotropic-wave effect. The results demonstrate that the vortex flow topology, developed at the later stages of the evolution, is dominated by one of these two effects dependent on the initial conditions. These two contrary effects of vorticity production were studied experimentally in more recent investigation[23] of the interaction between the heated bubble, generated by the OD in the focal point of a parabolic mirror, and the planar shock, induced by the reflection of the blast-wave in this mirror. As shown, when the reflected bow shock is not strong enough, the *reversal jet* appears and the effect of wave anisotropy is dominant, otherwise - the induced *direct jet* emerges and the baroclinic effect dominates. Similar processes are to be expected when two heated bubbles in quick succession interact with each other in supersonic flow upstream of the bow shock.

The current experimental and numerical investigation is aimed at further analysis of flow-field structure development at single- and double-pulse OD and their interaction with a hemispherical body. In particular, the influence of the distance between the discharge zone and the body, deposited energy level and time interval between subsequent pulses are investigated in the present paper. The most remarkable properties of the bow-shock / heated-bubble interaction, like the shock wave passage phenomena and the compression and deformation of the bubbles with formation of ring vortices downstream, are analyzed as resulting from the shock-accelerated spherical *light-gas* inhomogeneity. A very preliminary description of the present experimental and numerical results was given earlier in Ref. 24.

II. Wind tunnel, test models and measurement techniques

The experimental investigations were conducted in the Ludwieg Tube Facility at DLR Göttingen[25] at free-stream flow conditions corresponding to Mach 2 at a Reynolds number, based on the body's diameter, of 1.54×10^6: stagnation pressure of $1.8 \times 10^5\ Pa$ and stagnation temperature of $270\ K$. The Ludwieg Tube

Facility provides at Mach 2 a test section with a cross-section of $0.34\,m \times 0.35\,m$ and a run time of about $0.35\,s$.

The wind tunnel tests have been carried out using a simplified axially symmetric hemisphere-cylinder model with a diameter of $60\,mm$ and a length of $200\,mm$ at zero angle of attack. The optical discharge upstream of the hemisphere was induced by a focused laser beam, penetrating the test model along its longitudinal axis. The optical path of the laser beam is shown schematically in the Figure 5. Before this beam reaches the test section, it is reflected by an external mirror towards the wind-tunnel window. Through the optical channel entry on the cylindrical surface the beam hits the internal mirror and turns round along the longitudinal channel in the upstream direction to the converging lens device. The channel diameter inside of the model was at least $10\,mm$, so that the laser beam with approximately $9\,mm$ diameter was well-suited. The exchangeable convex lens was mounted on the axis of the model as flush as possible with the nose surface. The distance from the lens middle plane to the virtual nose position of the model (upstream stagnation point of the hemisphere) along the axis of symmetry was about $4\,mm$. The distance between the laser beam focal point and the virtual nose of the model was varied in the tests from $46\,mm$ up to $146\,mm$. Most measurements were made with a distance of $76\,mm$ (corresponding to a lens with a focal length of $80\,mm$).

A flash lamp pumped *Nd:YAG* laser *CONTINUUM Surelite PIV III* was used in the tests as the optical energy source. Two laser heads are mounted on a single compact platform, providing symmetrical output beams at $532nm$ for dual pulse applications. Both pulses have equivalent beam uniformity and pulse duration of approximately $5\,ns$ at $10\,Hz$ repetition rate. For the present investigations the special features of this laser system were used, which make it possible to change the output power of each laser head independently from the other up to $420\,mJ/pulse$ and to reduce the time delay between both pulses by external triggering with nanosecond precision from any desired value down to zero.

The laser beam energy transferred to the discharge region was varied as parameter in the present investigations. Careful calibration tests of whole set-up were made before and after the wind tunnel test campaign with a precision power meter. The laser-power measurements were made at different positions along the optical path. So the optical power was measured not only directly at the output shutter of the laser, but also at the position of the internal mirror of the model, to quantify the losses of energy on the way (possible losses due to reflection, transmission and emission). Furthermore, the power measurements after the optical discharge give information about the residual energy at different power levels, which could not be absorbed by the air or radiated by the light. The absorbed energy, which was spent in each of the runs only for flow heating, could be only roughly estimated considering these components. The problem is that the calibrations described could be made only at *wind-off* conditions in the test section. Consequently, the vibrations of some optical parts, which could appear during the tests, were not taking into account. Although all external optical components were mounted at a vibration-free area of the test hall that is decoupled by a separated fundament from the wind tunnel facility, the vibrations could cause additional energy losses. Furthermore, differences between the supersonic free-stream conditions and those in the calibration, and first of all the lower density in the oncoming flow, could have an influence on the absorbed energy level.

The standard shadowgraph technique was used in these investigations to visualize the effect of pulsed energy deposition. Recording of shadowgraph pictures was made at a constant frame rate of $30\,kHz$ and an exposure time of $2\,\mu s$ by a high-speed CMOS-camera *PHOTRON Ultima APX-RS 250K*. The intensive electromagnetic radiation, generated obviously by the optical discharge, shows a strong interference with the camera function, leading to the damage of the CMOS-chip in the first test phase. Only special measures, undertaken subsequently on the camera housing with the aim to protect the chip from the damaging radiation, could help to complete the investigations successfully. Unfortunately, the grounded protection grid, mounted for this reason between the camera head and the lenses, has influenced slightly the picture quality. The reason is that some parts of this grid, positioned near the focal plane of the optical set-up, work additionally as *Schlieren-knife-edge*. The effect of this *knife-edge* can be seen locally behind the bow shock wave on the obtained shadowgraph pictures.

III. Numerical technique

The numerical method employed[15,16] is based on a $2-D$ axisymmetric formulation of the Euler equations in conservative form and the perfect gas model. A Godunov-type method is used, in which numerical fluxes at the current time level were obtained by solving a local one-dimensional Riemann problem by the *HLLEM*

algorithm. Spatial third order accuracy is achieved using *MUSCL* reconstruction with min-mod limiter. The time integration is performed with the explicit third-order Runge-Kutta *TVD* scheme. The amount of energy per unit mass and unit time, supplied by ED, is modeled by a source term in the energy equation.[16] The grid size was 800×400 *points*, refined exponentially towards the axis of symmetry. According to experimental estimations, an ellipsoidal shape of the energy source with semiaxes of $1.0\,mm$ and $0.2\,mm$ in longitudinal and transversal directions correspondingly was chosen. The energy deposition time was set to $5\,ns$ as in the current experiments.

The used CFD-code was successfully validated earlier[13−16] by modeling a wide range of existing experiments: periodic pulsed OD in argon flow upstream of different bodies of revolution,[11] single-pulse OD upstream of a sphere in supersonic air flow,[17] and single-pulse OD in quiescent air.[26]

IV. Results and discussion

Three experimental series were performed in order to investigate the influence of the different pulse parameters on the flow (Figure 6). In the first series the energy level of the single-pulse ED at a distance of $76\,mm$ from the sphere was varied to 151, 264, 333, 548 and $666\,mJ$, in which the latter two values were achieved by simultaneous triggering of both laser heads (double-pulse OD at zero time delay). In the second series the effect of two pulses in quick succession with a time interval of $20\,\mu s$ was studied. Both pulses were focused in this case at the same distance L_{ED} of $76\,mm$, thereby the first pulse has a fixed energy level of $333\,mJ$ and the second one reduced amounts of $87\,mJ$ or $215\,mJ$. In the third series, both pulses had equal energy levels of $333\,mJ$ and the time delays between the pulses as well as the distance from the body were varied (Δt_{ED} to $10\,\mu s$ or $20\,\mu s$, L_{ED} to $46\,mm$ or $76\,mm$).

The numerical simulations were performed with the described parameters and are discussed together with the experimental data in the following subsections. Since in the experiments the camera was not synchronized with the laser pulse, the exact time of the first picture in each sequence is unknown, and only the frame rate is exactly known. Therefore, an approximate time was determined in each case by visual comparison of the computed sequence with the first shadowgraph in the experimental sequence. For this purpose positions of the heated bubble and of the blast wave were used for time fitting. As shown by comparison with experiments,[15] this technique is reliable concerning the prediction of spot and blast wave evolution in time. In accordance with the described methodology the best fit was achieved in each case in the numerical calculations when the distance between the body and discharge position L_{ED} was slightly reduced (e.g. $74\,mm$ instead of $76\,mm$) and the absorbed energy level was estimated to be only 50% of the value determined experimentally. This big difference in the levels of energy deposition, estimated in the experiments and needed in calculations, can be explained by the experimental uncertainties attributable to the initial volume-size of the energy deposition and to the energy amount absorbed in fact by the flow, as well as by the limitations of the simplified numerical modeling

A. Single pulse energy deposition

The results obtained by a single-pulse ED demonstrate the effect of energy level deposited into the flow at a fixed distance. An example of flow development in time is shown in Figure 7 by experimental shadowgraph pictures (left column) and by numerical predicted distributions of the density gradient (right column, top part) and of the vorticity (right column, bottom part) in the longitudinal cut-plane. It stands to reason that the visualization of the CFD results by density gradient distributions in a single cut-plane used here is not identical to the shadowgraph pictures obtained experimentally because the shadowgraph technique helps to visualize the spatial averaged density gradients along the whole optical path in the span-wise direction.

The spherical blast wave, emerged by the initial thermal spot expansion and seen in the first picture (a) at circa $30\,\mu s$ after the laser pulse ($t = 30\,\mu s$), encounters the body at $t \approx 97\,\mu s$ (b). The flow structure shortly after the bow-shock transit across the heated bubble, resulting in the so-called *lens-effect*, is clearly visible at $t = 130\,\mu s$ (c). The unsteady initial shock refraction during its transmission through a gaseous inhomogeneity is known to be observed when an incident shock is crossing the bubble surface owing to the change in sound speed.[18] Since the local Mach number inside of the heated bubble in the present case is even subsonic, the strong Mach2-bow-shock moves very fast upstream as soon as it bumps into the heated spherical bubble and the transmitted shock wave develops a convex curvature. The passage of the shock wave through the bubble is accompanied by the *precursor shock wave*, which emerges inescapable outside of

the inhomogeneity[27] and results in a λ-shock structure at the junction. The gas-dynamic properties, typical for the λ-structure (triple point, Mach stem and slip line), can be seen in the calculated flow field also after shock transit at $t = 163\,\mu s$(d), where furthermore some crossing secondary shock waves directly upstream of the nose can be observed. These waves are generated during the shock passage due to the reflection of the bow shock on the interior bubble surface, which acts like convex mirror and focuses the re-transmitted waves along the axis of symmetry. This effect was predicted earlier numerically as typical for spherical heated bubbles,[12] as well as for laser-induced OD.[16]

The last two pictures in Figure 7(e, f) show the following formation of a vortex ring and its impingement on the body further downstream. The vorticity generation at the shock / light-bubble interaction occurs as a result of the baroclinic misalignment[28] of the existing density gradient and the shock-induced pressure gradient. This mechanism is obviously responsible also for the formation of vortex rings in the investigated flows (e, f), in which the density gradient is induced by pulsed local heating. The processes of compression and deformation of the heated bubble with subsequent formation of a vortex ring, observed here, are very similar to those known from investigations of shock-accelerated inhomogeneous flows.[18,28] The formation of thin vorticity sheets, generating at the bow-shock/heated-bubble interaction, is visualized in the bottom parts of each calculated flow-field diagram (Figure 7, right column). In the later stages of the flow development they are transformed into the long-living vortex rings traveling downstream. The clockwise rotation of these vortices is marked by the red, and the counterclockwise rotation by the blue colors.

Additional details of the flow development at this energy level are delivered by the Figure 8, where the calculated total pressure (left column) and temperature (right column) flow-field distributions are shown. With variation of the energy level, the scales of flow-field-specific structures change correspondingly. That is visible in the next two figures, where the similar sequences of the flow-field transformation by single-pulse ED are presented for energy levels of 151 mJ (Figure 9) and 666 mJ (Figure 10). To give a quantitative conclusion to the effect of different energy levels, several characteristic scales were measured from the resulting experimental and numerical pictures. So, the most upstream bow shock distance, observed in experiments shortly after the shock transit the bubble, was at 151 mJ of ca. 11.5 mm (or 19% of body's diameter D), for 333 mJ about 14 mm ($\approx 0.233D$) and for 666 mJ about 13.5 mm ($\approx 0.225D$). The cross-sizes (diameters) of the bubbles were thereby ca. 17 mm, 19 mm and 23 mm respectively. The numerical results follow this trend, although the typical sizes are overpredicted by ca. $1 - 2\,mm$. The mentioned effect of energy-level raise is demonstrated additionally in Figures 11 and 12 by the calculated static and total pressure fields at given times before the interaction (left column, $t = 30\,\mu s$) and shortly after the bow shock transit (right column, $t = 130\,\mu s$).

Furthermore, the case of the lower energy level (Figure 9) demonstrates the existence of a secondary vortex ring at the later phase of flow evolution predicted numerically. The formation of secondary and tertiary vortex rings in the post-shock flows is known also from SBI investigations (cp. Figure 3, d) as typical for interactions with strong shock waves.[21] The short distance between the shock front and the body's nose seems to be the reason that this phenomenon occurs seldom in bow-shock/heated-bubble interacting flows.

The time-history of the pressure distribution on the nose as well as the influence of the deposed energy level are visible in the Figure 13, where the pressure-time diagram at the upstream stagnation point of the body, obtained in numerical calculations, is shown. The annotated peaks (B, C and D) correspond approximately to the stages shown in Figure 7 (b, c, d). The effect of deposited energy level on the normalized-pressure record is surprisingly not really pronounced. The shown evolution of the wall pressure in time is in contrast very exciting. It indicates very-well the effects, originated during the mutual transit of the heated bubble and the bow shock wave.

The first peak B in the surface pressure record (Figure 13) is clearly caused by the blast wave, which reaches the sphere at $t \approx 97\,\mu s$. After reflection of the blast wave from the model surface the gas near the body undergoes, as expected, a short over-expansion and the following re-compression by secondary shock/compression waves. This behavior is well-known from investigations of the blast wave propagation and reflection (see e.g. Refs. 29, 30) and has been predicted also for the case of laser energy deposition in a quiescent air.[13,26] As shown there, the front of the expanding cylindrical/spherical blast wave is followed by expansion waves, causing a pressure decrease down to levels less than the undisturbed one, and finally by a secondary shock wave attending the re-compression. In our case, the peak C in the pressure-time diagram at $t \approx 130\,\mu s$ is caused by the impingement of this secondary re-compression shock at the model stagnation point. The new and rapid pressure drop between the peaks C and D appears due to the impingement of the *reflected rarefaction waves*, coming from the interaction zone as a result of the suction effect, caused by the

deformation of the bubble (cp. Figure 3, b). The last peak D occurs due to the hitting of the *re-transmitted reflected shock wave*, which is originated by the reflection of the bow shock from the bubble's inner surface (cp. Figure 3, c). The quantitative comparison of the pressure jumps at peaks B and D shows clearly that the mentioned re-transmitted reflected shock wave seems to be three to four times stronger than the blast wave.

From this point of view, different surface-pressure time-histories on the model nose should be expected for some possible combinations of distances and levels of ED, as well as flow conditions. For instance, the variation of L_{ED} or E_{ED} changes, first of all, the relative position of the characteristic peaks. So, at bigger distances L_{ED} and higher energy levels E_{ED} the time interval between the peaks B and D increases. Thereby, if the pressure jump at the peak B decreases with bigger L_{ED}, the intensity of the reflected shock at the peak D is practically independent from this parameter. Application of very short distances L_{ED} leads e.g. to the vanish of the local peak C. That is the reason for qualitatively other pressure-time diagrams, discussed earlier in Ref. 16. The explanations given there for the cause of the stagnation-point pressure variations with time could be completed in the present work with theses new results.

B. Double pulse energy deposition

An example of flow evolution by two subsequent ED pulses is shown in Figure 14. The second pulse, which deposited a reduced energy of $87\,mJ$ at $\Delta t_{ED} = 20\,\mu s$ after the first one, creates an additional heated bubble close by the first spherical blast wave (a). The initiation and propagation of both blast waves lead to a new type of bubble interaction: the interaction of each heated bubble with the blast wave, induced by the other discharge. These interactions are weaker than the major bow-shock interaction, but the effects, observed at short distances between both bubbles, are very similar. As result of these interactions one or both heated bubbles demonstrate a intensive vortex ring evolution still before the main interaction with the bow shock takes place. The opposite direction of the blast wave transmissions (a) leads to the converging of the heated bubbles to each other and to the formation of a vortex configuration like a *double mushroom*(b). The numerical simulation predicts this interaction passably good, but it tends to distinguish ring vortex structures upstream of the interaction more clearly.

The evolution of bubbles in the wind-tunnel tests shows in some cases the emergence of low-speed jets along the axis of symmetry before the bow-shock interaction (see e.g. Figure 14, b, c) that occurs typically in laser-induced bubbles due to energy-source anisotropy. The formation of this secondary flow seems to be accelerated by the additional baroclinic effect, induced by the blast wave, when the direction of the oncoming blast-wave agrees with the laser-beam direction. The hypothesis about the possibility to eliminate the jet flow by means of the reversal passage of the blast wave through the heated bubble,[23] could not be confirmed in these tests. That is demonstrated by the shadowgraph images presented in Figure 15. The heated-air bubble, generated in the experiments by the first laser-pulse, shows a clear jet flow aligned towards the body, even though the traveling direction of the blast wave produced by the second OD, is penetrating the heated bubble in the opposite direction (b).

Although the flow structure before the interaction differs from the single pulse significantly, the global properties of the bow-shock/heated-bubbles interaction are very similar to that of single-pulse interaction discussed above (c-f). The agreement of the experimental and numerical results became more worse with increasing energy level for the second pulse to $215mJ$ and especially to $333\,mJ$ (Figure 15). The differences are observed already at the stage of the bubbles development before the interaction (b) and in the larger bow-shock displacement at later stages (c, d). The influence of the subsequent ED pulse in the experiment is mainly expressed in diffusing of the ring-vortex structure after the interaction, caused probably by the turbulent mixing, which is not accounted for by the employed numerical model.

The last series of double pulse experiments demonstrates effects of distance L_{ED} and time delay Δt_{ED}. For this series at a high energy level in both pulses of $333\,mJ$ only some qualitative comparisons could be done because the numerical prediction does not work well in this case. The influence of the distance is illustrated in Figure 16, where experimental and computed flow fields are shown at instants of the encounter of the heated bubble and the bow shock. In case of $L_{ED} = 46\,mm$, both blast waves are rather strong when they impinge the body (a, b). The difference in the calculated lens effects for both distances L_{ED} can be seen in the following pictures (e, f). Obviously, the simulation overpredicts the lens effect.

The effect of time delay Δt_{ED} is demonstrated in Figure 17. For the smaller delay the second blast wave disappears during the time of interaction and both thermal spots coalesce (a, b). In the experiment the interaction is quite similar for both delays (cp. Figure 17, d and Figure 15, d), but numerical simulation

shows significant differences in the size and in the structure (Figure 17, e, f).

C. Small-scale vortex structures in heated bubbles

The appearance of the RM-instability in flows with light-gas or pulse-heated bubbles is mainly caused by the geometry-given spherical shape of the their interface. As shown, the baroclinic vorticity generation leads to formation of vortex rings in the final phases of the flow evolution. The scales of these vortex structures are related to the whole cross-sectional sizes of the existing inhomogeneities and could be identified as *macro* structures.

Analysis of some published investigations of the interaction of shock waves with laser-pulse-heated bubbles shows that there is apparently another occurrence of this instability, which is to be found in a clearly smaller dimension. The appearance of secondary periodic small-scale vortices near the heated-bubbles downstream of the bow shock has been observed already experimentally[17] (Figure 18, a, c, e) and later numerically[16](b, d, f). This phenomenon was not explained in the cited papers, but, from the point of view, based on the ideas of RM-instability, the cause of these vortices can be the small-scale waviness of the bubble's interface. Different shape deviations from the ideal-contour can results from the anisotropic effects,[22,30] occurring in the initial phase of the bubble explosion.

The waviness of the bubble's interface is a possible source of the baroclinic vorticity generation due to the *"perturbed interface"* between two gases of different densities (cp. Figure 2). The low-amplitude disturbances of the bubble interface are revealed in the first shown shadowgraph-image, describing the earlier phase of the interaction (Figure 18, a). The impulsive compression of the bubble due to the shock passage causes a further growth of initial perturbations (shape waviness), and the interface becomes unstable. This instability can additionally be stimulated by the reflected blast- and secondary shock-waves, hitting the bubble interface at the later stages of evolution. Consequentially, the vortex sheet rolls up and the periodic longitudinal vortices emerge in the periphery of the compressed bubble downstream of the bow shock. The existence of longitudinal vortices in the interaction zone can clearly be seen in the last both shadowgraph-images (c, e). The computations demonstrate signs of distinct RM-instability of the interface of the compressed heated bubble (d, f), which can be considered as a source of the mentioned longitudinal vortex structures.

V. Conclusions

The performed investigation highlights the influence of various parameters characterizing the laser-induced ED on the flow topology. The variation of these parameters can lead to different time histories concerning the induced pressure distribution on the body's surface. For instance, the variation of L_{ED} or E_{ED} change, first of all, the relative position of the characteristic peaks. So, at bigger distances L_{ED} and higher energy levels E_{ED} the time interval between the peaks B and D increases. Thereby, if the pressure jump at the peak B decreases with bigger L_{ED}, the intensity of the reflected shock at the peak D is practically independent from this parameter. Application of very short distances L_{ED} leads e.g. to a vanishing of the local peak C.

As expected, the scales of interaction are increased at higher energy levels deposited to the flow. Some significant topological properties of the bow-shock / heated-bubble interaction, like shock passage and reflection, as well as the evolution of the heated bubble into a vortex ring downstream and the particularity in the pressure-time diagram on the nose of the blunt body can be described as a part of shock-accelerated spherical *light-gas* inhomogeneity flows.

The evolution and interference of the bubbles created by double-pulse heating show the influence of the weak blast waves, penetrating neighboring bubbles and stimulating therewith vorticity generation. As an indicator for this influence, the low-speed jets, emerging along the axis of symmetry due to energy-source anisotropy, were analyzed. The formation of these secondary flows seems to be accelerated by the additional baroclinic effect, induced by the external blast wave, coming from the second pulse, when its direction agrees with the laser-beam direction. The idea to eliminate the jet flow by means of the reversal passage of the blast wave through the heated bubble could not be confirmed in these tests.

The *waviness* of the bubble's interface is identified as an additional source of the baroclinic vorticity generation. The existence of the longitudinal vortices in the interaction zone, observed in some published former investigations, is explained as resulting from the RM-instability of the interface of the compressed heated bubble.

Acknowledgments

The first author thanks Karsten Pfeiffer from the DNW Ludwieg Tube Wind Tunnel staff for assistance in executing the experiments and Martin Rein from the DLR Institute of Aerodynamics and Flow Technology for helpful discussions.

References

[1]Maurer F., Brungs W. "Influencing the Drag and the Bow Wave by Heat Addition in the Stagnation Point of Blunt Bodies in Supersonic Flow," VII^{th} Congress of Flight Sciences (ICAS): Proc. Munich, Germany, Sept. 1968 (Jahrbuch 1968 der DGLR). P. 174-189 (In German).

[2]Chernyi G. G. "Some Recent Results in Aerodynamic Applications of Flows with Localized Energy Addition," AIAA-99-4819, 1999.

[3]Bityurin V., Klimov A., Leonov S. "Assessment of a Concept of Advanced Flow/Flight Control for Hypersonic Flights in Atmosphere," AIAA-99-4820, 1999.

[4]Zheltovodov A. A. "Development of the Studies on Energy Deposition for Application to the Problems of Supersonic Aerodynamics," Preprint No. 10-2002, Institute of Theoretical and Applied Mechanics, Russian Academy of Sciences, Siberian Branch. Novosibirsk, 2002, 43 p.

[5]Knight D., Kuchinskiy V., Kuranov A., Sheikin E. "Survey of Aerodynamic Flow Control at High Speed by Energy Deposition," AIAA-2003-0525, 2003.

[6]Fomin V.M., Tretyakov P.K., Taran J.-P. "Flow Control Using Various Plasma and Aerodynamic Approaches (Short Review)," *Aerospace Science and Technology*, 2004, No. 8, pp. 411-421.

[7]Zubkov A.I. Garanin A.F., Safronov V.F., Sukhanoskaya L.D., Tretyakov P.K. "Supersonic Flow Fast an Axisymmetric Body with Combustion in Separation Zones at the Body Nose and Base," Thermoph. and Aeromech., 2005, Vol. 12, No. 1, pp. 1-12.

[8]Bletzinger P., Ganguly B.N., Van Wie D., Garscadden A. "Plasmas in High Speed Aerodynamics," *J. Phys. D: Appl. Phys.*, Inst. Phys. Publ., 2005, Vol. 38, pp. R33-R57.

[9]Georgievsky P. Yu., Levin V. A. "Supersonic Flow over Bodies in the Presence of External Energy Input," *Pisma v Zhurn. Teh. Phiz.*, 1988, Vol. 14, No. 8, pp. 684-687 (in Russian).

[10]Borzov V.Yu., Mikhailov V.M., Rybka I.V., Savishenko N.P., Yuriev A.S. "Experimental Research of Supersonic Flow over the Obstacle at the Energy Supply into the Undisturbed Flow," *Inzh.-Phyz. Zhurn.*, 1994, Vol. 63, No.5, pp. 515-520 (in Russian).

[11]Tretyakov P.K., Garanin A.F., Grachev G.P., Krainev V.L., Ponomarenko A.G., Tishenko V.N., Yakovlev V.I. "The Supersonic Flow Control over the Bodies with the Use of Power Optical Pulsating Discharge," *Dokladi Akademii Nauk (DAN)*, 1994, Vol. 351, No. 3, pp. 339-340 (in Russian).

[12]Georgievsky P. Yu., Levin V. A. "Unsteady Interaction of a Sphere with Atmospheric Temperature Inhomogeneity at Supersonic Speed," *Fluid Dynamics*, 1993, 28(4), pp. 568574 (Translated from *Mehanika Zhidkosti i Gaza*, 1993, No. 4, pp. 174-183).

[13]Zheltovodov A. A., Pimonov E.A. "Streamwise Vortex/Shock Wave Interaction in Energy Deposition Conditions," Intern. Conf. on the Methods of Aerophys. Research: Proc. Pt. II, Novosibirsk, 2004, pp. 237-245.

[14]Knight D., Yan H., Candler G., Kandala R., Zheltovodov A.A., Pimonov E. "Control of Normal Shock by Pulced Energy Deposition," Proc. of the 15^{th} Int. Conf. on MHD Energy Conversion and the 6^{th} Int. Workshop on Magneto-Plasma Aerodynamics, Ed. V.A. Biturin, Moscow, IVTAN, 2005, Vol. 2, pp.514-524.

[15]Zheltovodov A. A., Pimonov E.A. "Numerical Research of Supersonic Flow Features in Conditions of Localized Energy Deposition and Verification of Calculations," Intern. Conf. on the Methods of Aerophys. Research: Proc. Pt. I, Novosibirsk, 2007, pp. 236-246.

[16]Zheltovodov A.A., Pimonov E.A., Knight D.D. "Energy Deposition Influence on Supersonic Flow over Axisymmetric Bodies," AIAA-2007-1230, 2007.

[17]Adelgren R., Yan H., Elliott G., Knight D., Beutner T., Zheltovodov A. "Control on Edney IV Interaction by Pulsed Laser Energy Deposition," *AIAA-Journal*, 2005, Vol. 43, No. 2, pp. 256-269.

[18]Niederhaus J.H.J., Greenough J.A., Oakley J.G., Ranjan D., Anderson M.H., and Bonazza R. "A Computational Parameter Study for the Three-Dimensional Shock-Bubble Interaction," *J. Fluid Mech.*, 2008, Vol. 594, pp.85-124.

[19]Zabusky N.J. and Zeng S.M. "Shock Cavity Implosion Morphologies and Vortical Projectile Generation in Axisymmetric Shock - Spherical Fast/Slow Bubble Interactions," *J. Fluid Mech.*, 1998, Vol. 362, pp.327-346.

[20]Aure R., Jacobs J. W. "Particle Image Velocimetry Study of the Shock-Induced Single Mode Richtmyer-Meshkov Instability," *Shock Waves*, 2008, Vol. 18, No. 3, pp. 161-167.

[21]Niederhaus J.H.J., Ranjan D., Oakley J.G., Anderson M.H., Greenough J.A., and Bonazza R. "Computations in 3D for Shock-Induced Distortion of a Light Spherical Gas Inhomogeneity," 26^{th} International Symposium on Shock Waves, $ISSW$2007, 15.-20.07.2007, Göttingen (Germany), 2007.

[22]Svetsov V., Popova M., Rybakov V., Artemiev V. and Medveduk S. "Jet and Vortex Flow Induced by Anisotropic Blast Wave: Experimental and Computational Study," *Shock Waves*, 1997, No.7, pp.325-334.

[23]Sasoh A., Mori K. and Ohtani T. "Richtmyer-Meshkov Instability in Laser Plasma-Shock Wave Interaction," 26^{th} International Symposium on Shock Waves, $ISSW$2007, 15.-20.07.2007, Göttingen (Germany), 2007.

[24]Schülein E., Zheltovodov A.A., Pimonov E.A. and Loginov M.S. "Experimental and Numerical Study of the Shock Wave Transformation by Laser-Induced Energy Deposition," Intern. Conf. on the Methods of Aerophys. Research: CD-Proc., Novosibirsk, 2008, 10 p.

[25]Ludwieg H., Hottner Th., Grauer-Carstensen H. "Der Rohrwindkanal der Aerodynamischen Versuchanstalt Göttingen, *Jahrbuch 1969 der DGLR*, 1970, pp. 52-58.

[26]Yan H., Adelgren R., Bogushko M., Elliott G., Knight D. "Laser Energy Deposition in Quiescent Air," *AIAA-Journal*, 2003, Vol. 41, No. 10, pp. 1988-1995.

[27]Henderson L.F. "The Refraction of a Plane Shock Wave at a Gas Interface," *J. Fluid Mech.*, 1966, Vol. 26, pp.607-637.

[28]Haas J.-F. and Sturtevant B. "Interaction of Weak Shock Waves with Cylindrical and Spherical Inhomogeneities," *J. Fluid Mech.*, 1987, Vol. 181, pp.41-76.

[29]Podlubnyi V. V., and Fonarev A. S. "Reflection of a Spherical Blast Wave from a Planar Surface," *Fluid Dynamics*, Nov. 1974, Vol. 9, No. 6, pp. 921-926.

[30]Liang S.-M., Hsu J.-L., and Wang J.-S. "Numerical Study of Cylindrical Blast-Wave Propagation and Reflection," *AIAA-Journal*, 2001, Vol. 39, No. 6, pp. 1152-1158.

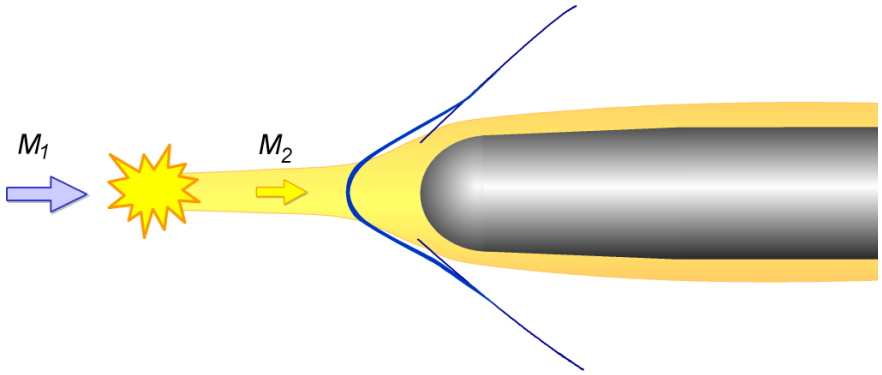

Figure 1. Effect of the localized flow heating upstream of a supersonic blunt body

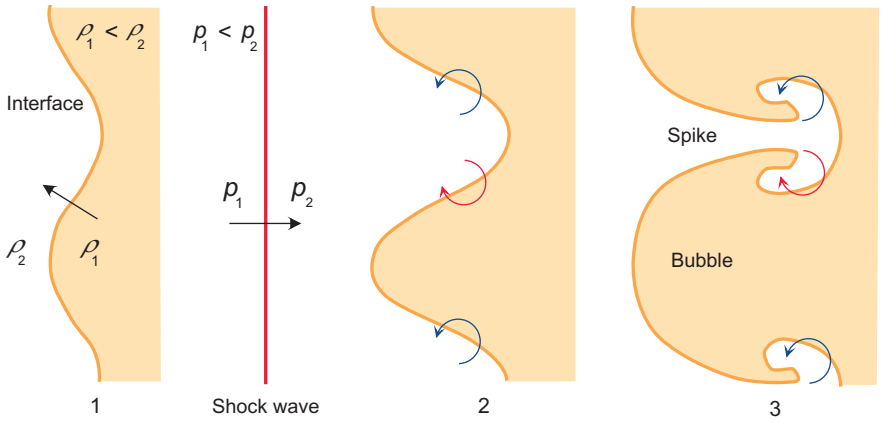

Figure 2. Three stages in the evolution of the RM-instability:[20] interface before shock interaction (1), vorticity deposited by shock interaction (2), and the resulting bubble/spike configuration after the shock transit (3)

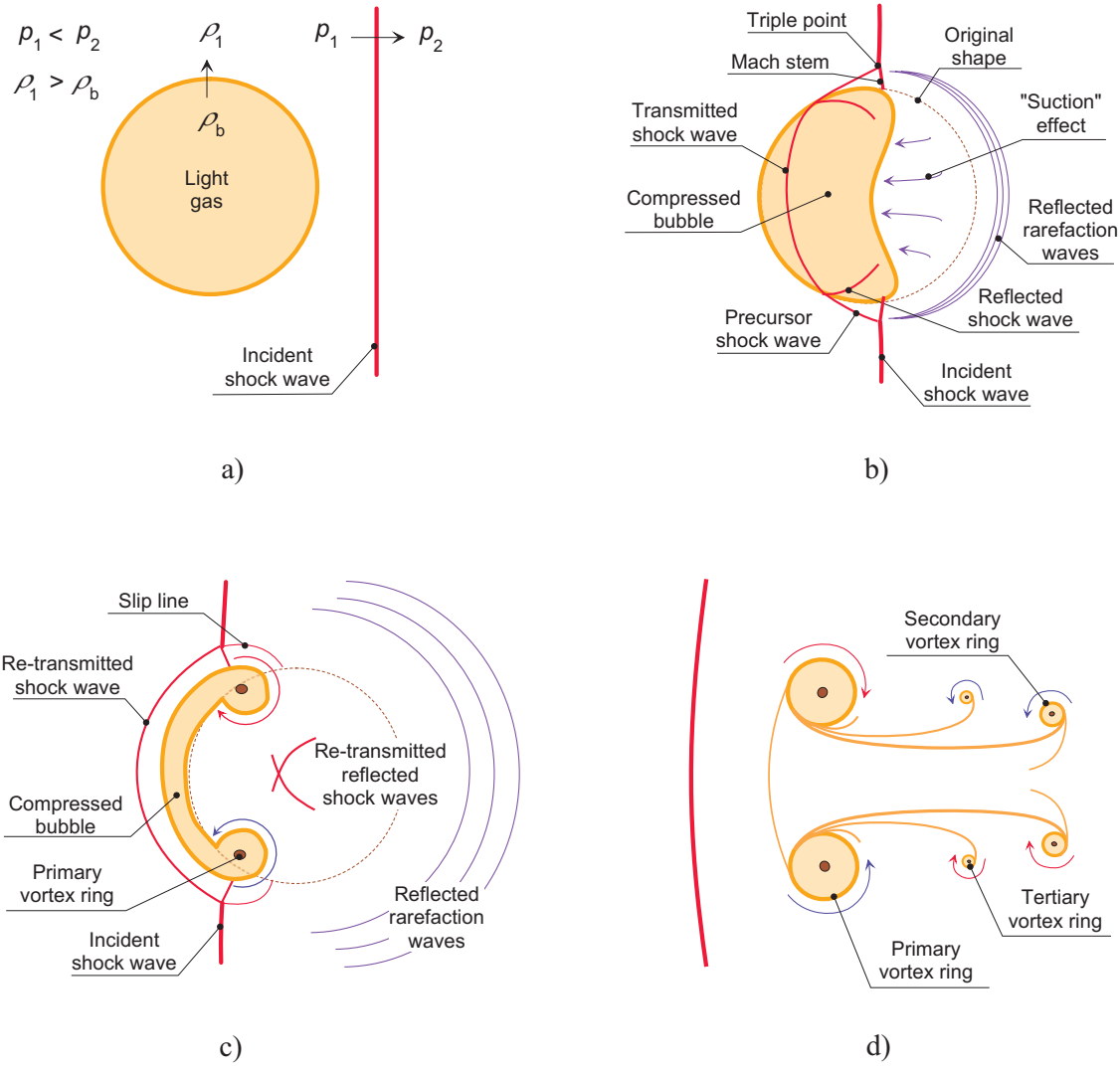

Figure 3. Schematic view of the shock/light-bubble interaction corresponding to results presented by Niederhaus et al.:[18,21] (a) before the interaction, (b) during initial shock wave transit, (c) shortly after this process, and (d) late phase of the flow development

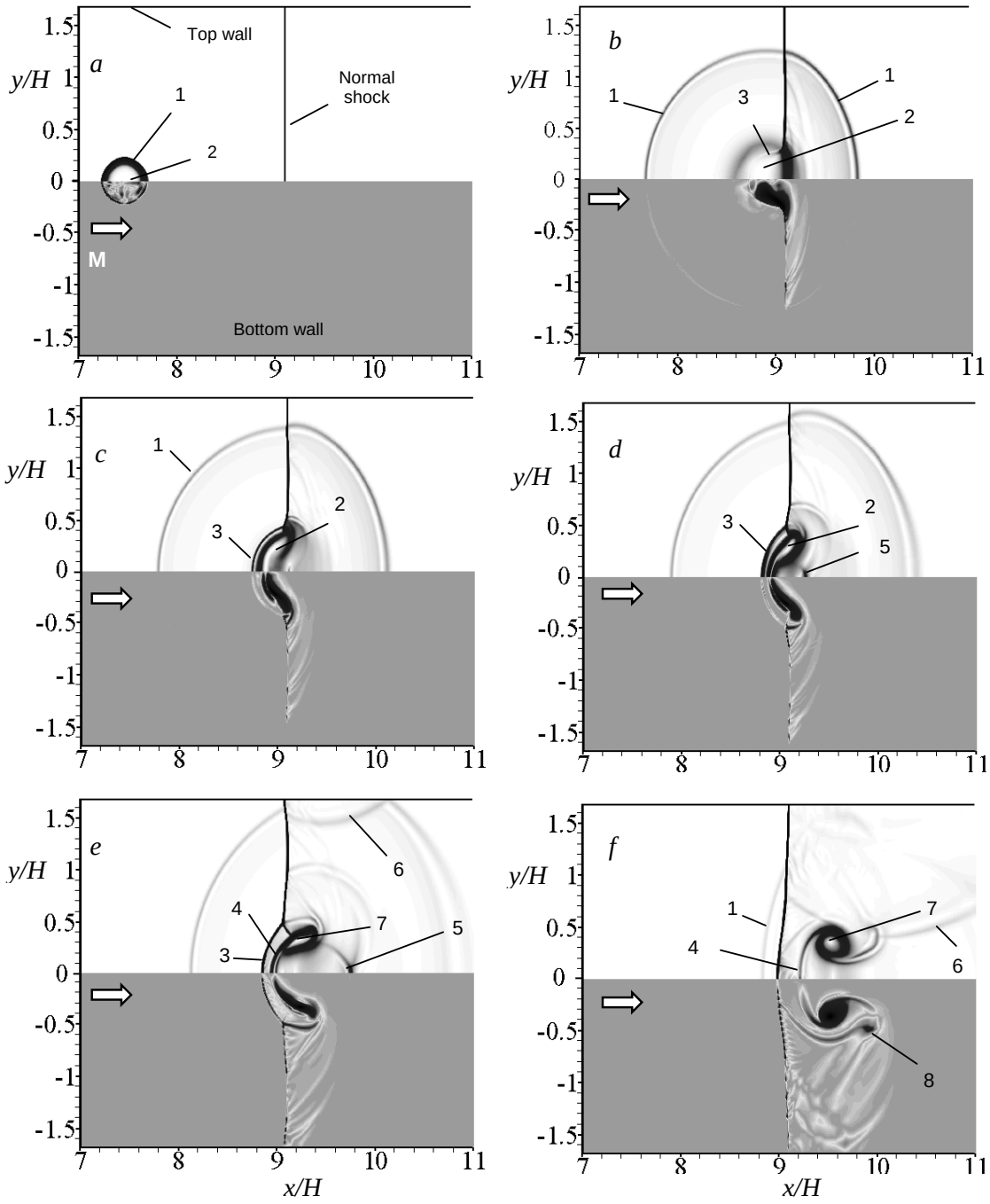

Figure 4. Interaction of a normal shock wave with the laser-pulse-heated air bubble in a 2-D channel at M_∞ = 2 and ϵ_{ED} = 100: density gradients (top part) and the vorticity (bottom part); 1 - blast wave, 2 - the heated bubble with reduced density, 3 - transmitted shock wave, 4 - compressed heated bubble, 5 - re-transmitted reflected crossing shock waves, 6 - shock wave reflected from the channel wall, 7 - primary vortex ring, 8 - secondary vortex ring

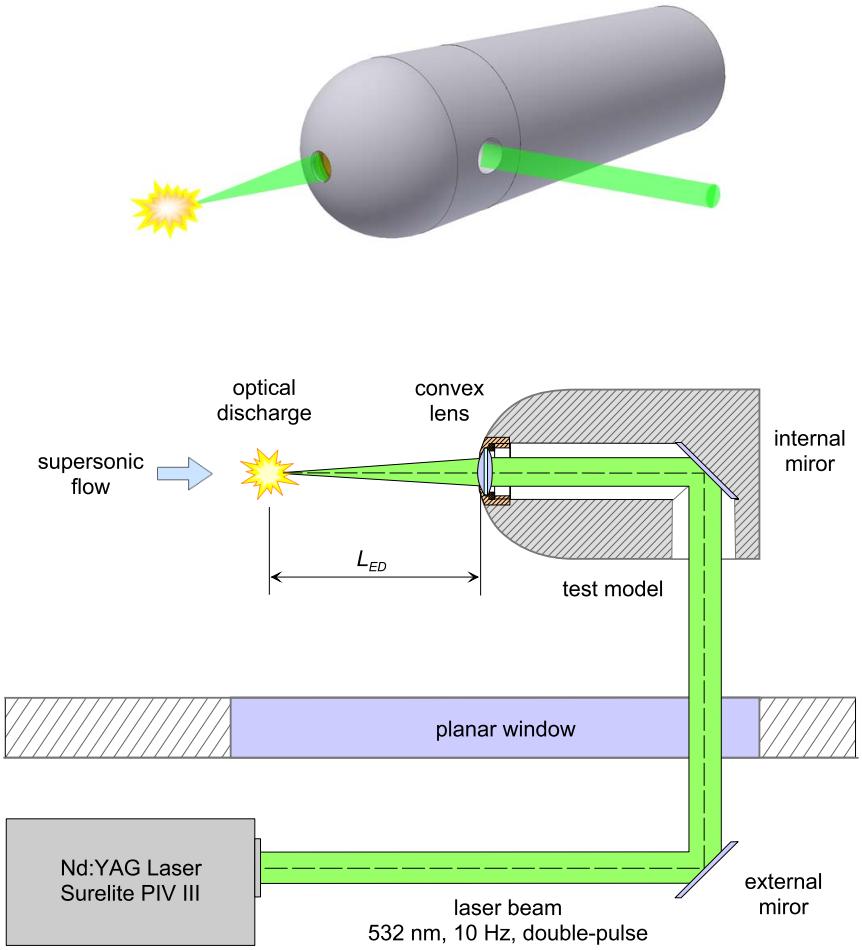

Figure 5. Set-up of the optical energy deposition experiment

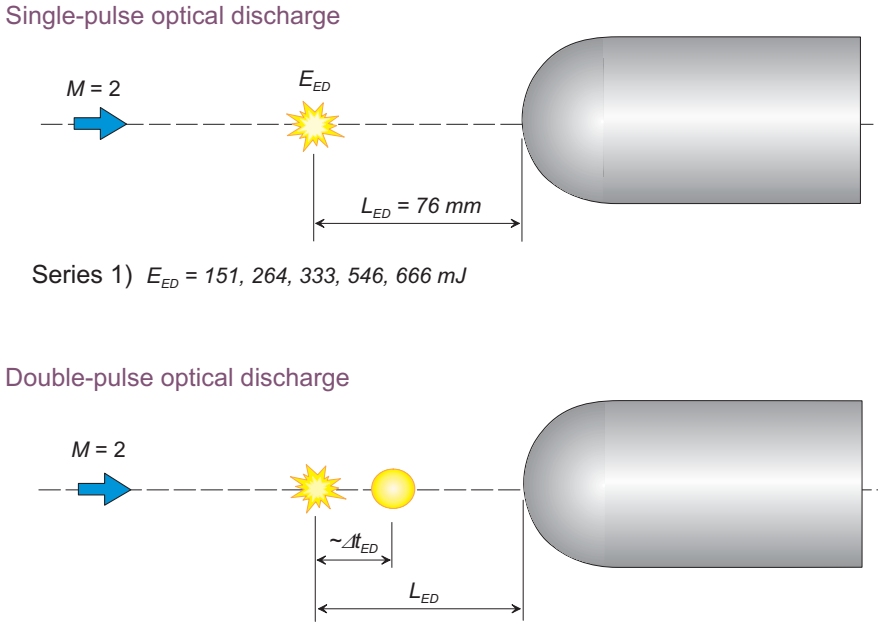

Figure 6. Investigated test cases

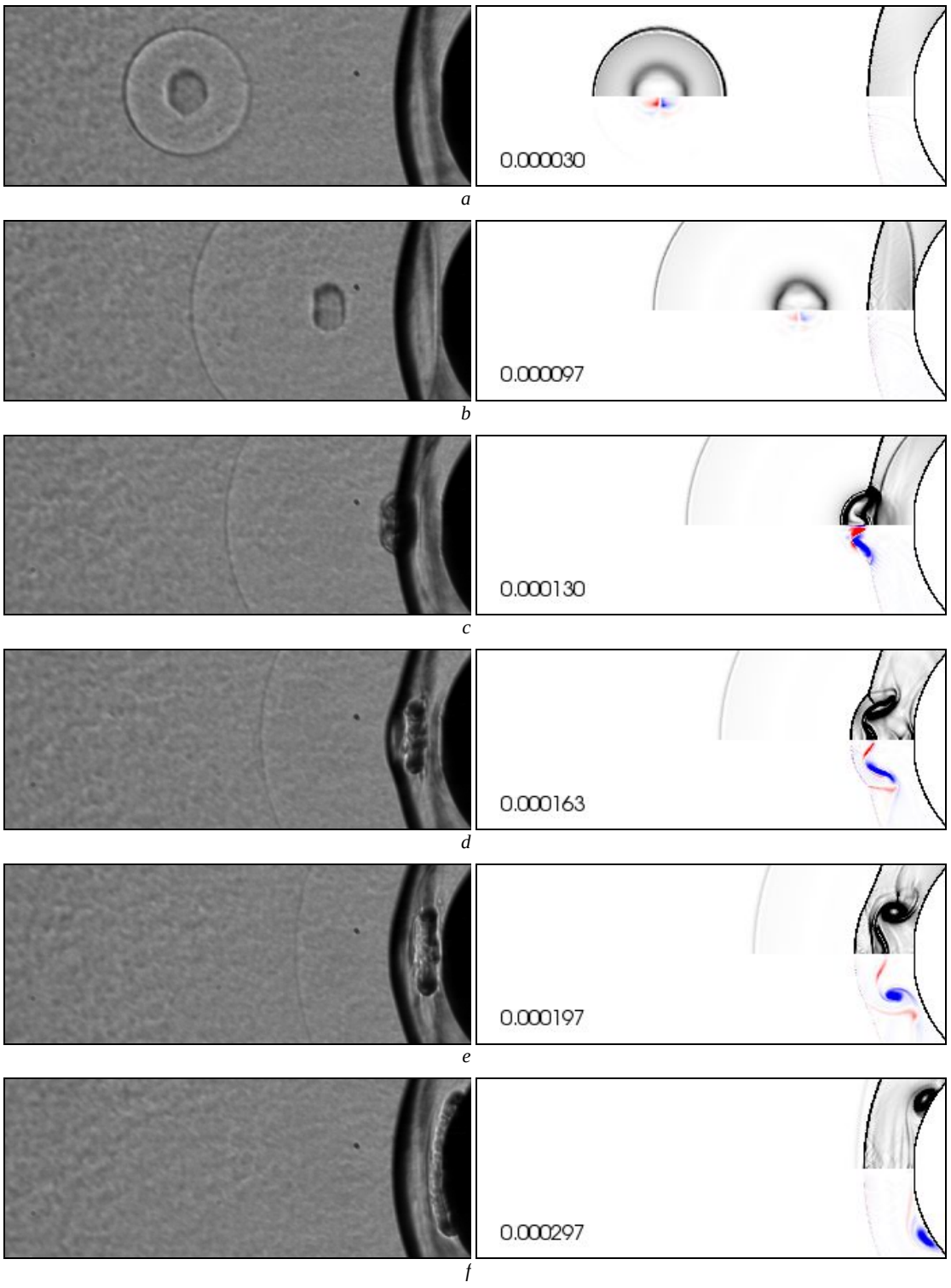

Figure 7. Experimental flow shadowgraphs (left column), as well as calculated density gradients (right colum, top part) and vorticity (right colum, bottom part) of a single pulse with energy of $333\,mJ$ ($L_{ED} = 76\,mm$)

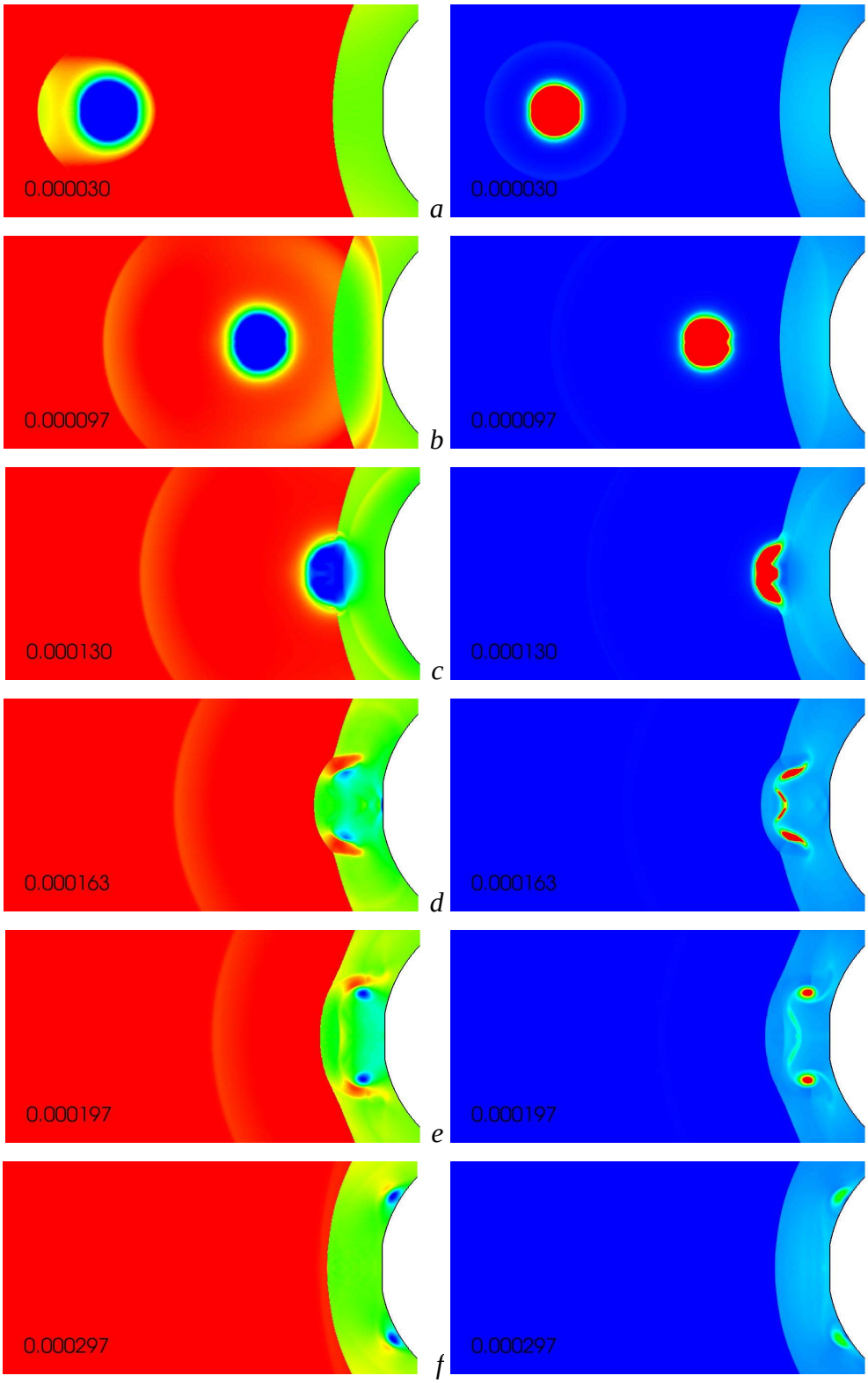

Figure 8. Total pressure (left column) and temperature (right column) of a single pulse with energy of $333mJ(L_{ED} = 76\,mm)$

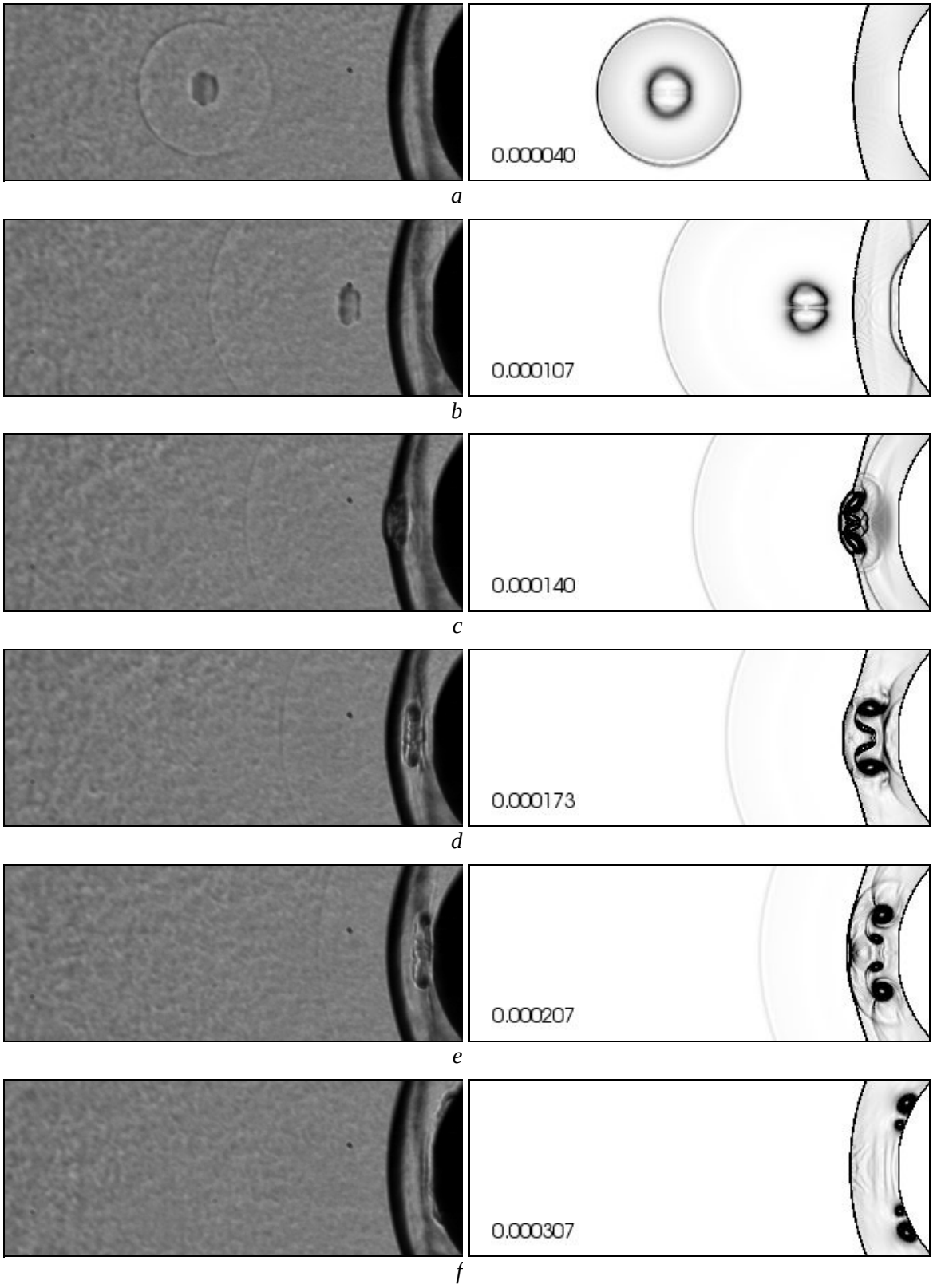

Figure 9. Experimental flow shadowgraphs (left column) and calculated density gradients (right column) of a single pulse with energy of $151\,mJ$ **(**$L_{ED} = 76\,mm$**)**

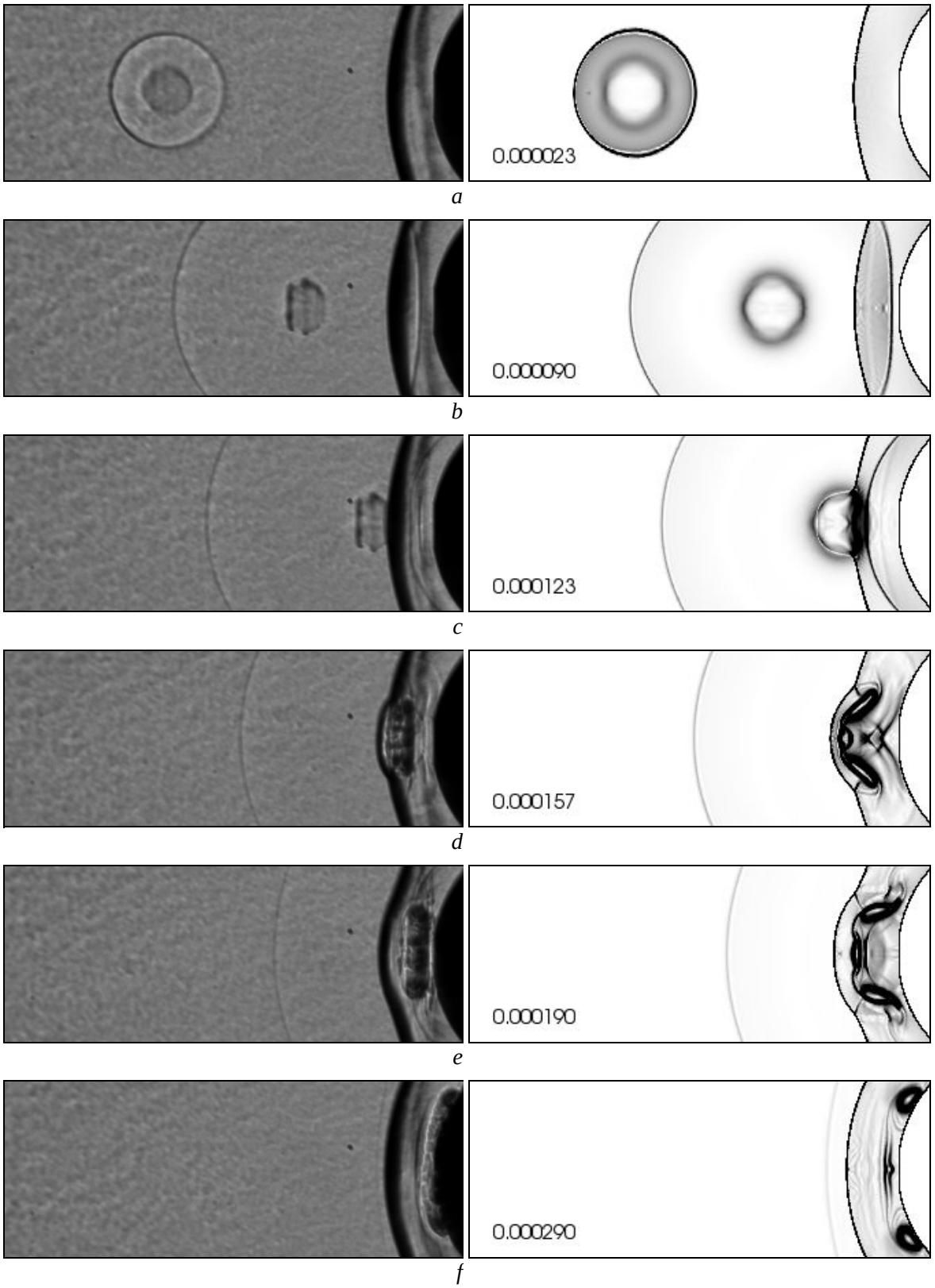

Figure 10. Experimental flow shadowgraphs (left column) and calculated density gradients (right column) of a single pulse with energy of $666\,mJ$ **(**$L_{ED} = 76\,mm$**)**

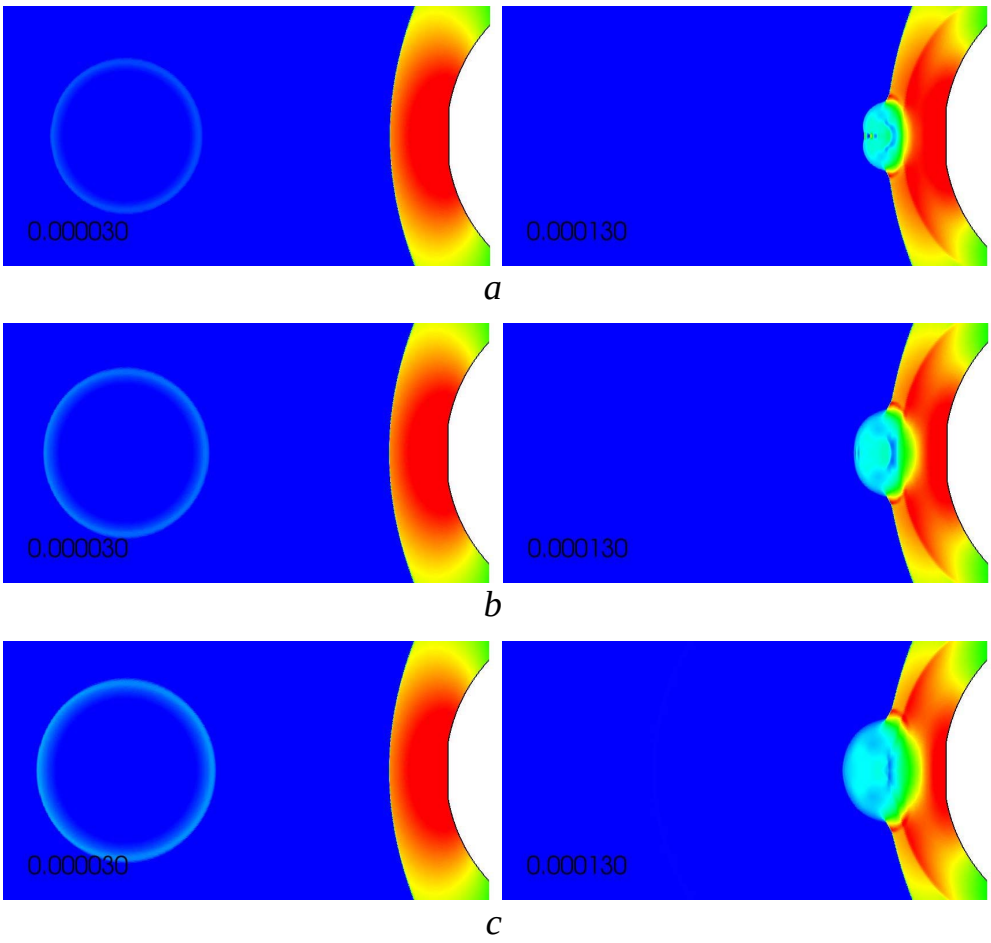

Figure 11. Static pressure field before (left column) and during interaction (right column) with energy values of: a- $151\,mJ$**, b-** $333\,mJ$ **and c-** $666\,mJ$ $(L_{ED} = 76\,mm)$

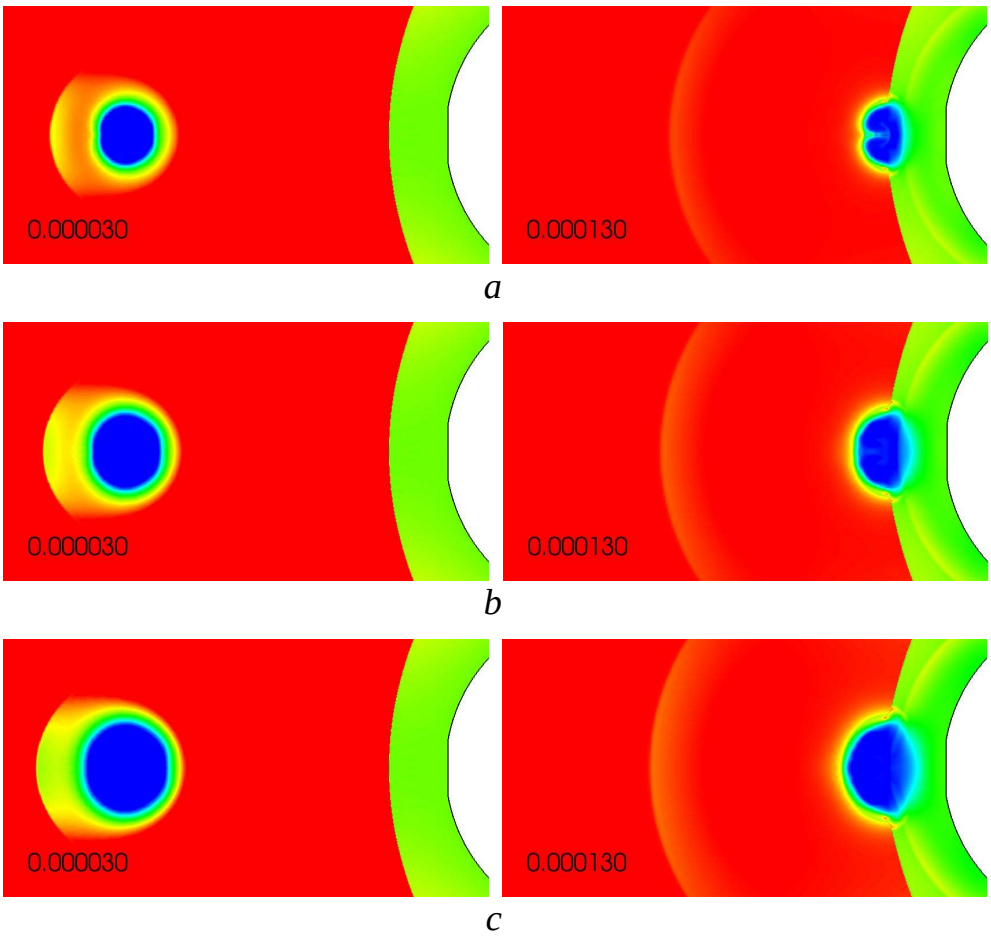

Figure 12. Total pressure field before (left column) and during interaction (right column) with energy values of: a- $151\,mJ$**, b-** $333\,mJ$ **and c-** $666\,mJ$ **(**$L_{ED} = 76\,mm$**)**

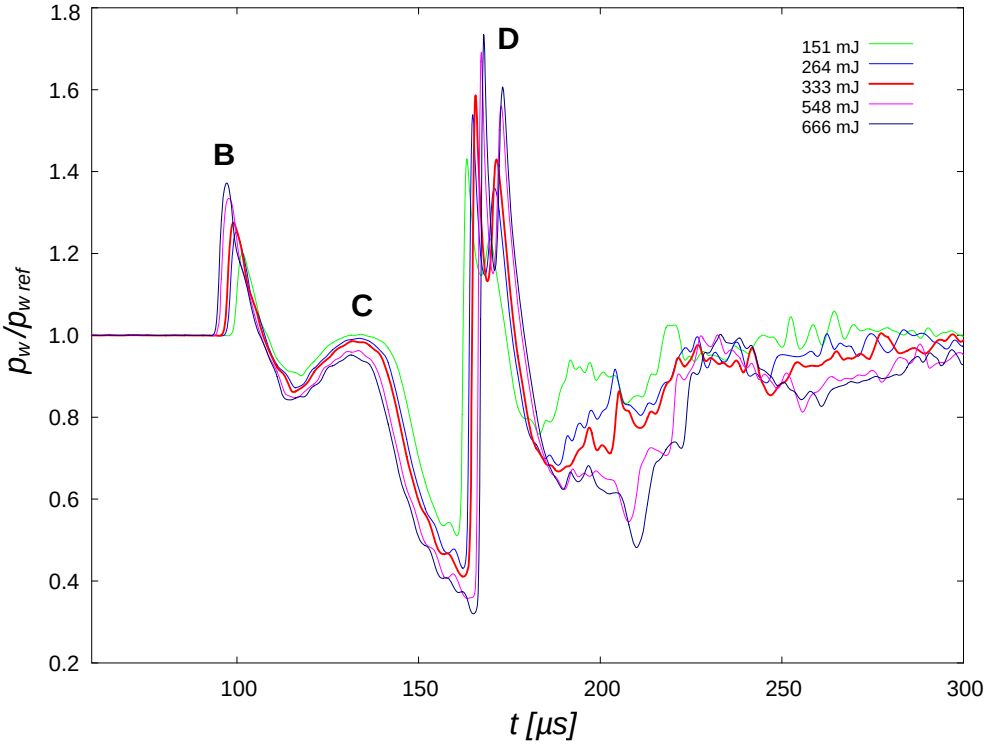

Figure 13. Time-history of pressure at stagnation point on the sphere for single pulse at different energy levels ($L_{ED} = 76\,mm$)

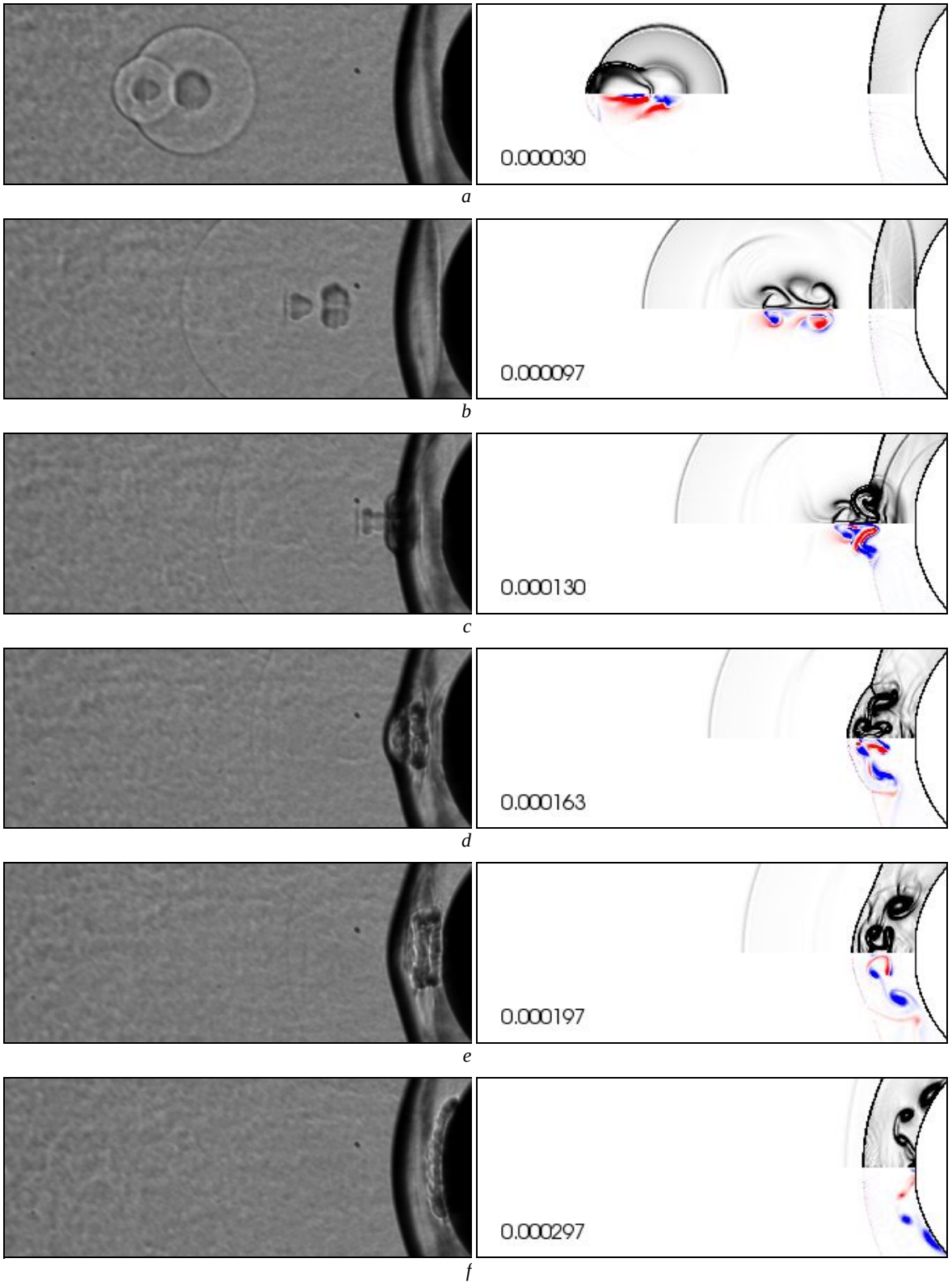

Figure 14. Experimental flow shadowgraphs (left column), as well as calculated density gradients (right colum, top part) and vorticity (right colum, bottom part) of a double pulse flow at energy of $333\,mJ$ **and** $87\,mJ(L_{ED} = 76\,mm,\ \Delta t_{ED} = 20\,\mu s\ )$

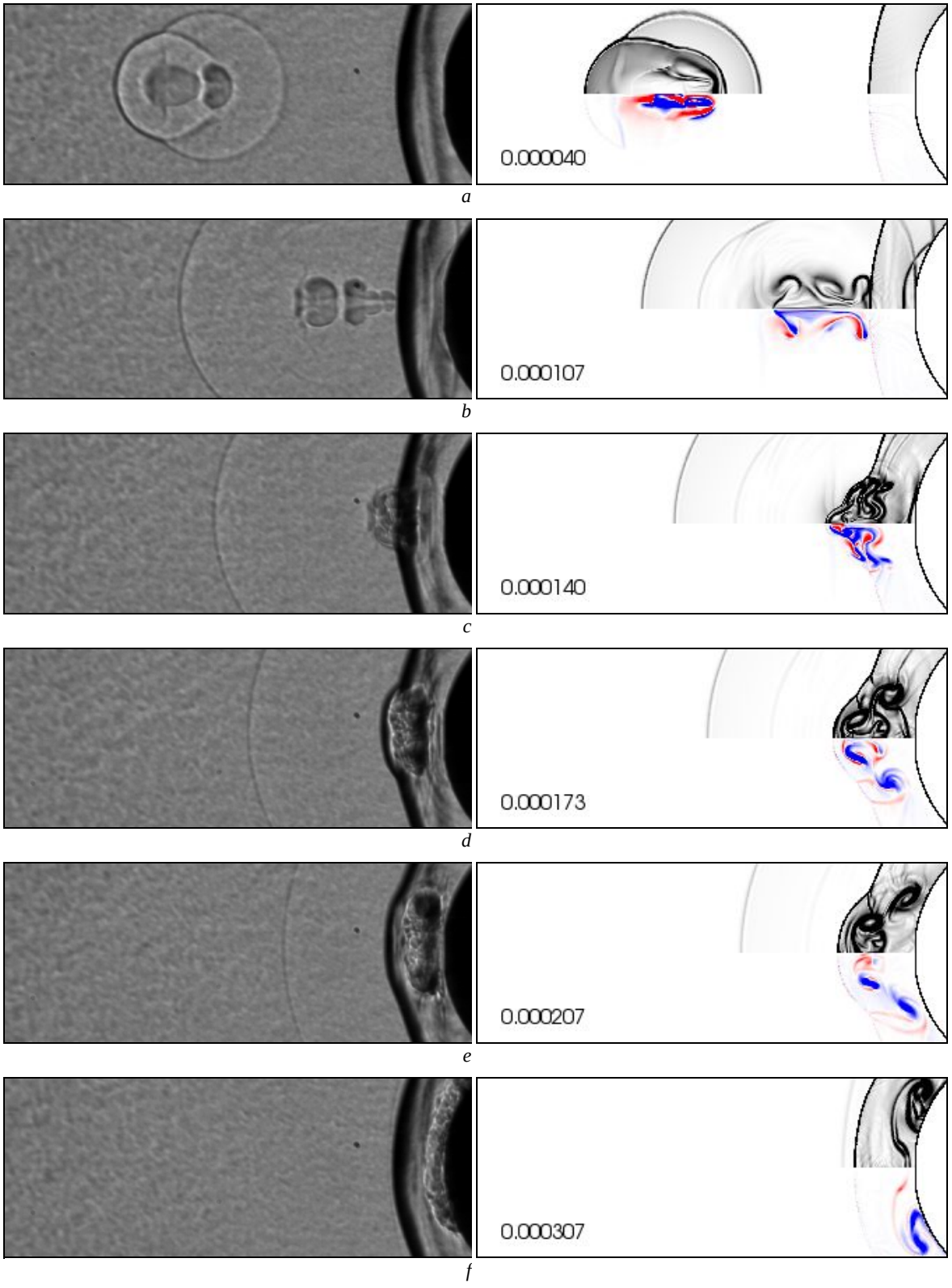

Figure 15. Experimental flow shadowgraphs (left column), as well as calculated density gradients (right colum, top part) and vorticity (right colum, bottom part) of a double pulse flow at energy-levels of $333mJ$ **(**$L_{ED} = 76mm$**,** $\Delta t_{ED} = 20\,\mu s$ **)**

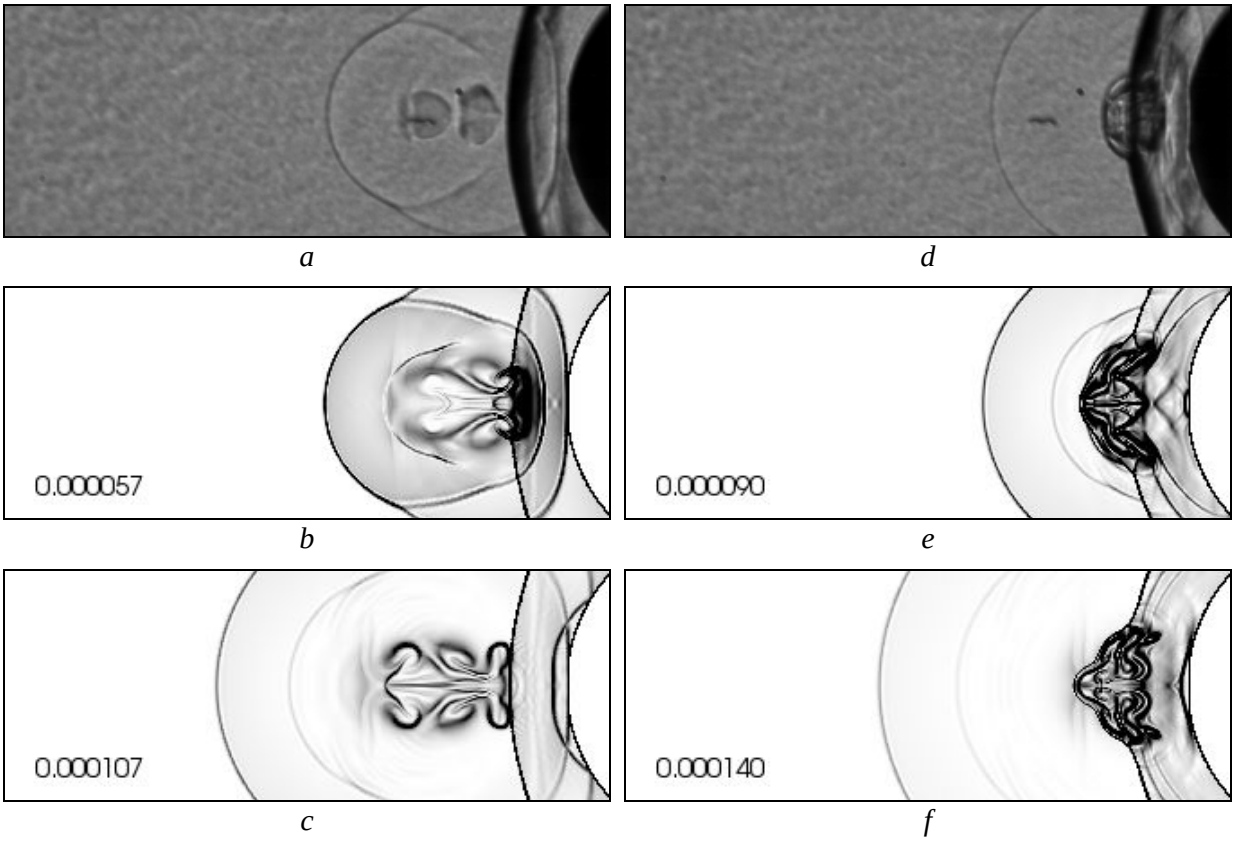

Figure 16. Flow structure of a double pulse flow at $E_{ED} = 333mJ$ and $\Delta t_{ED} = 20\mu s$ at the start of the interaction (left column) and during the lens effect (right column): a, d - experimental pictures for $L_{ED} = 46\,mm$; b, e - corresponding pictures from simulation; c, f - simulation for $L_{ED} = 76\,mm$

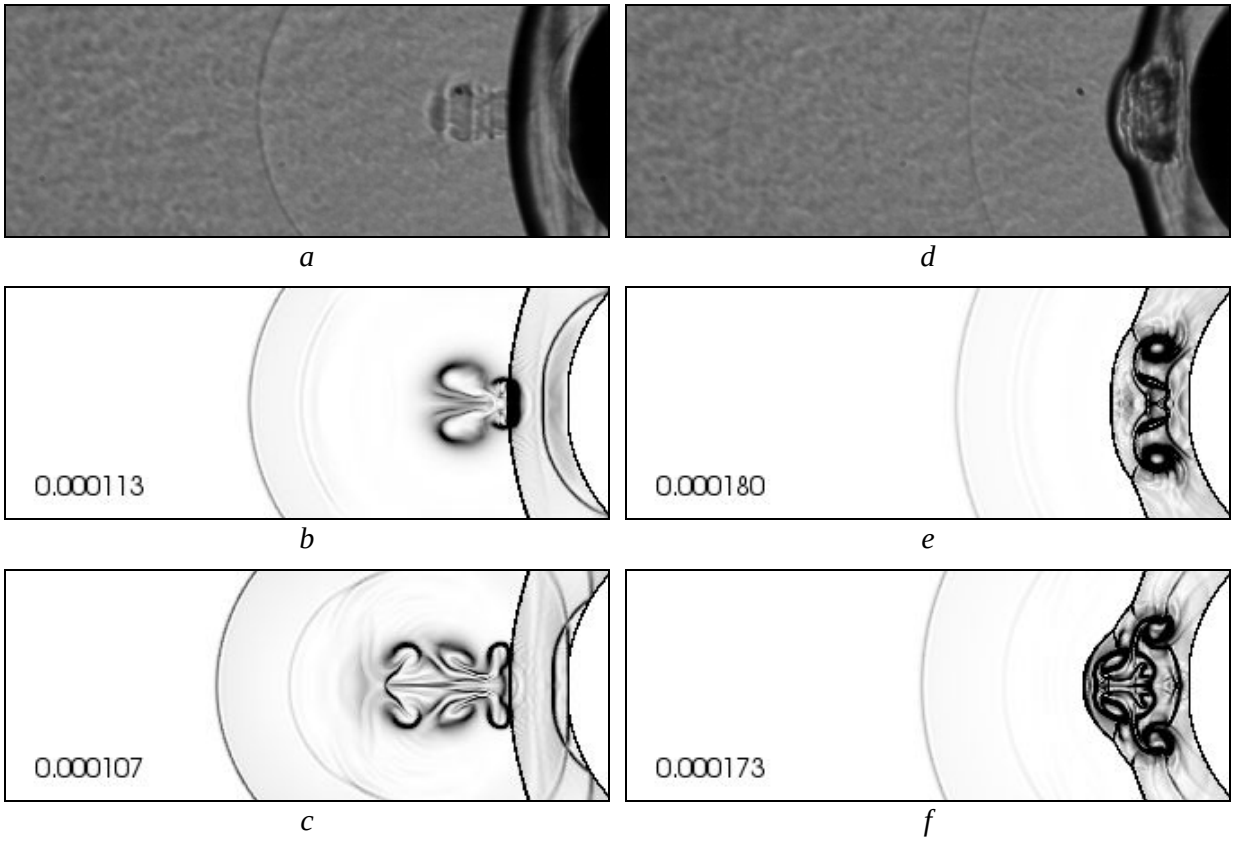

Figure 17. Flow structure of a double pulse flow at $E_{ED} = 333mJ$ and $L_{ED} = 76mm$ at the start of the interaction (left column) and during the lens effect (right column):a, d - experimental pictures for $\Delta t_{ED} = 10\,\mu s$; b, e - corresponding calculated pictures; c, f - simulation for $\Delta t_{ED} = 20\,\mu s$

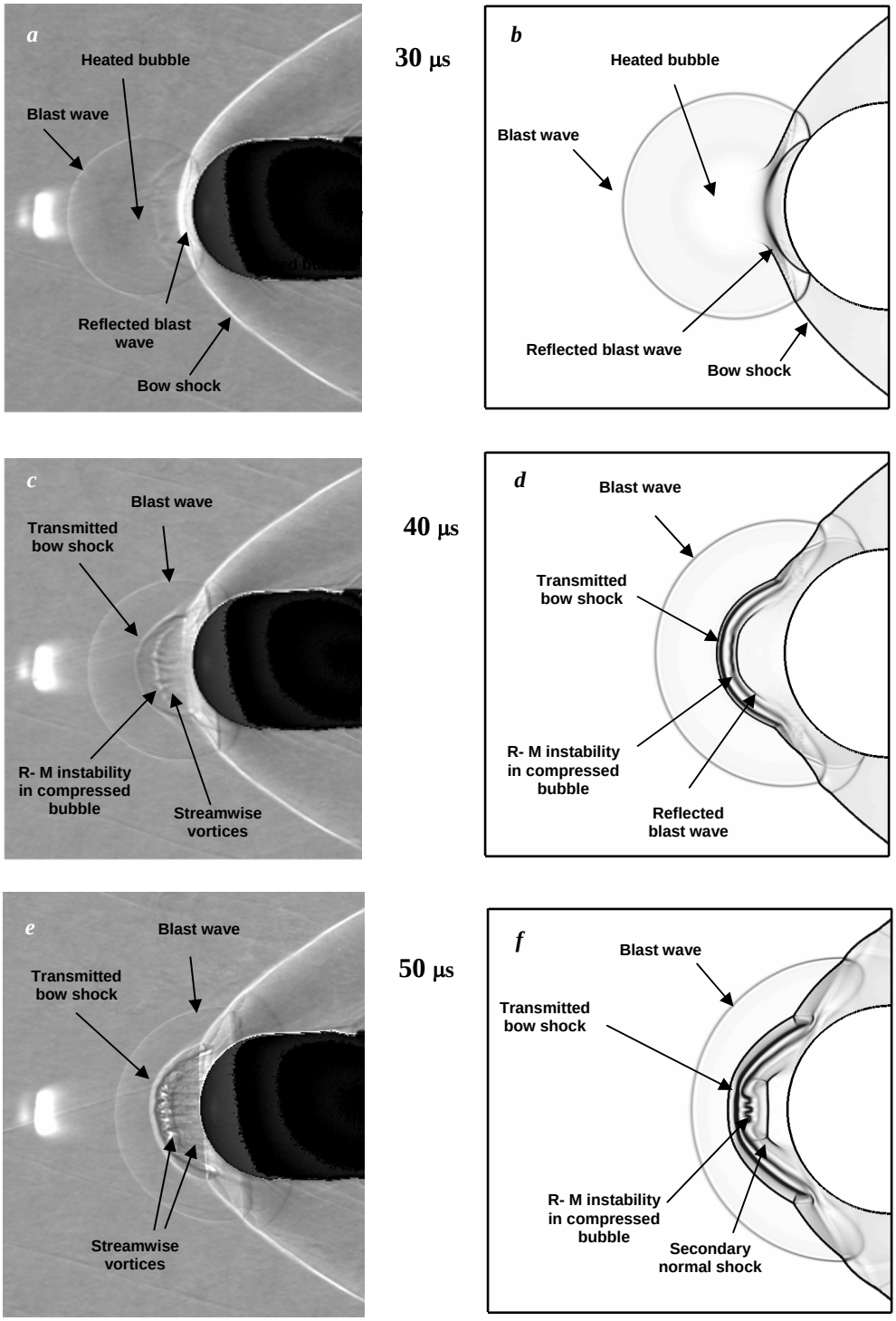

Figure 18. Small-scale vortex structures in pulse-heated bubbles past a sphere at $M = 3.45$ (deposited energy $E_{ED} = 289\,mJ/Pulse$): a, c, e - experimental shadowgraph images from Ref. 17; b, d, f - computed density gradients in vertical cut-plane from Ref. 16